NANO LETTERS

pubs.acs.org/NanoLett Letter

A RuCoBO Nanocomposite for Highly Efficient and Stable Electrocatalytic Seawater Splitting

Le-Wei Shen,[‖] Yong Wang,[‖] Jiang-Bo Chen, Ge Tian, Kang-Yi Xiong, Christoph Janiak, David Cahen, and Xiao-Yu Yang*

Cite This: *Nano Lett.* 2023, 23, 1052−1060 Read Online

ABSTRACT: Efficient and stable electrocatalysts are critically needed for the development of practical overall seawater splitting. The nanocomposite of RuCoBO has been rationally engineered to be an electrocatalyst that fits these criteria. The study has shown that a calcinated RuCoBO-based nanocomposite (Ru_2Co_1BO-350) exhibits an extremely high catalytic activity for H_2 and O_2 production in alkaline seawater (overpotentials of 14 mV for H_2 evolution and 219 mV for O_2 evolution) as well as a record low cell voltage (1.466 V@10 mA cm^{-2}) and long-term stability (230 h @50 mA cm^{-2} and @100 mA cm^{-2}) for seawater splitting. The results show that surface reconstruction of Ru_2Co_1BO-350 occurs during hydrogen evolution reaction and oxygen evolution reaction, which leads to the high activity and stability of the catalyst. The reconstructed surface is highly resistant to Cl^- corrosion. The investigation suggests that a new strategy exists for the design of high-performance Ru-based electrocatalysts that resist anodic corrosion during seawater splitting.

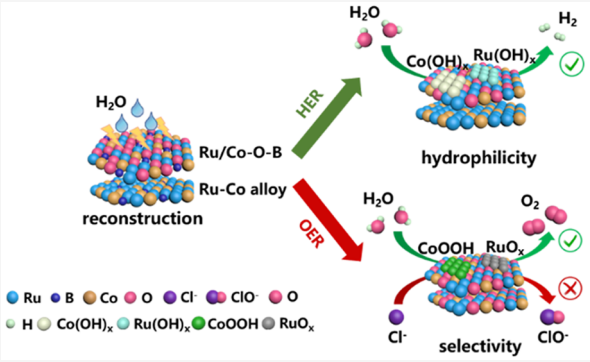

KEYWORDS: *Ru-based electrocatalysts, multifunctional sites, surface reconstruction, directed transformation, electrocatalytic seawater splitting*

Electrolysis of seawater for hydrogen (H_2) and oxygen (O_2) generation can be of great significance in the context of storing green electrical energy as green chemical energy.[1,2] However, many issues need to be addressed in making this process applicable to large-scale employment, needed for an impact on the global energy supply and consumption. Such issues include corrosion of electrocatalysts and complicated side reactions that occur in seawater owing to its high salinity and complex composition.[3,4] Ruthenium (Ru) has been shown to display remarkable resistance to seawater-induced corrosion and high electrocatalytic activity for the hydrogen and oxygen evolution reactions (HER and OER).[5,6] Importantly, high potentials that exist during practical electrocatalytic processes often result in overoxidation of Ru to form water-soluble Ru oxides (e.g., RuO_4).[7,8] Moreover, the instability of Ru under high potentials is heightened by its coordination with chloride ion (Cl^-), which is present in high concentrations in seawater. Thus, this ion accelerates structural destruction and anodic corrosion of Ru.[9,10]

According to the Pourbaix diagram of Ru- and Ru-based oxide species in aqueous solution,[11,12] applied potentials that are compatible with stable oxidation states of Ru oxides are under ∼1.4 V in acidic (pH = 0) or ∼0.5 V in alkaline (pH = 14) electrolyte, respectively, and the thermodynamic potential of OER is 1.23 V. Thus, the Ru oxides are more likely to be overoxidized to unstable RuO_4 during OER, if the OER overpotentials are much higher than ∼170 mV. Moreover, the oxidation potentials for Ru metal are even lower (∼0.5 V at pH = 0 or ca. −0.4 V at pH = 14). Unfortunately, to the best of our knowledge, Ru-based materials with overpotentials less than 170 mV for OER have not been reported even though many strategies have been explored to decrease the overpotential of Ru-based materials, such as heteroatom doping,[13,14] alloying engineering,[15−17] interface engineering,[18,19] and confinement.[20,21] Therefore, it is of great scientific interest and technological importance to develop approaches to decrease the overpotential as much as possible and enhance the stability of Ru-based materials at the same time.

Nano ruthenium−cobalt (RuCo) alloying has been widely used to create electrocatalysts; however, this process does not prevent overoxidation of Ru and anode corrosion during OER, especially in seawater splitting.[22,23] Boronization is an efficient method to regulate the performance of alloys, and transition-

Received: November 28, 2022
Revised: January 24, 2023
Published: January 27, 2023

https://doi.org/10.1021/acs.nanolett.2c04668
Nano Lett. 2023, 23, 1052−1060

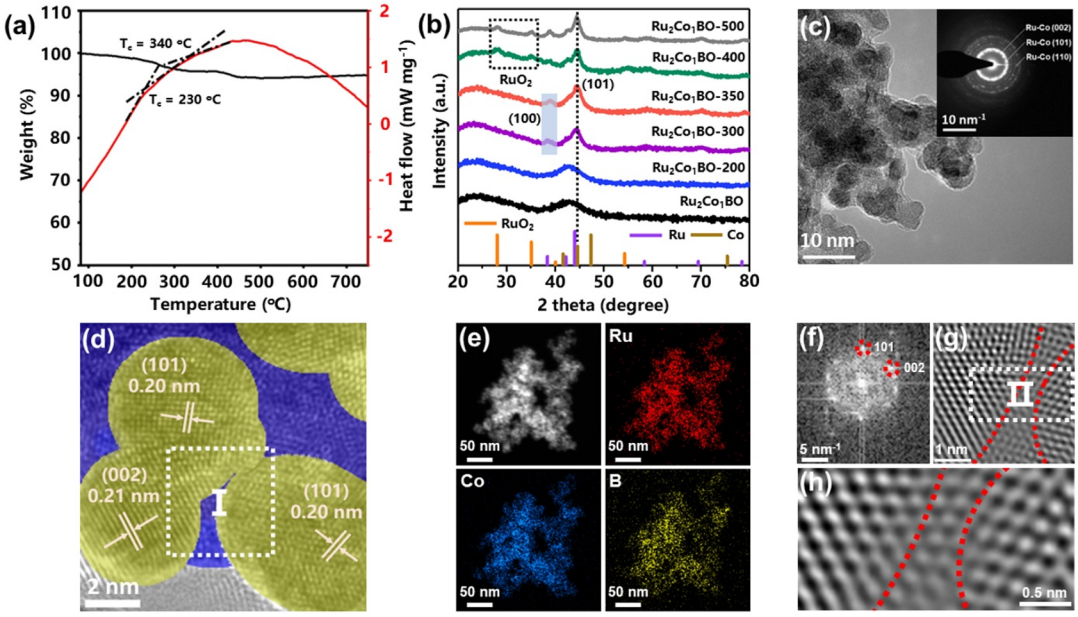

Figure 1. (a) TG-DSC analysis of as-prepared Ru_2Co_1BO, in argon. (b) XRD patterns of as-prepared Ru_2Co_1BO, Ru_2Co_1BO-200, Ru_2Co_1BO-300, Ru_2Co_1BO-350, Ru_2Co_1BO-400, and Ru_2Co_1BO-500. (c) TEM image of Ru_2Co_1BO-350; the inset is the corresponding SAED pattern. (d) HRTEM of Ru_2Co_1BO-350 nanoparticles. (e) HAADF-STEM image of Ru_2Co_1BO-350 and EDS mapping images of Ru, Co, and B. (f) Diffraction pattern of region I in Figure 1d from FFT. (g) Inverse FFT image of diffraction pattern in Figure 1f, showing the crystal fusion region between the Ru_2Co_1BO-350 nanoparticles. (h) Magnified image of region II in Figure 1g.

metal borides/borates are efficient and stable for water splitting.[24,25] But it needs to be pointed out that the boronization process requires high-temperature annealing (often >800 °C), which can lead to nanostructure aggregation and block formation, both of which cause decreases in electrocatalytic activity.[26,27]

Herein, we developed a low-temperature (<400 °C) calcination method to fabricate RuCoBO nanocomposites, denoted as Ru_xCo_yBO-T, where T is the calcination temperature. In this effort, we observed that nanocomposites (Ru_2Co_1BO-200−400) generated by calcination at temperatures of 200−400 °C have outstanding electrocatalytic activities and durabilities in overall seawater splitting. Among these, in alkaline seawater (1.0 M KOH + 3.5% wt. NaCl), Ru_2Co_1BO-350 displays the best performance (HER, 14 mV and OER, 219 mV). An electrolyzer comprised of this catalyst has a record low cell voltage of 1.466 V at 10 mA cm^{-2} and long-term stability up to 230 h at 50 and 100 mA cm^{-2}. Furthermore, a sun light-driven electrocatalytic system with Ru_2Co_1BO-350 as the electrode promotes seawater splitting with a Faraday efficiency of ∼98.6%.

The Ru_xCo_yBO precursors were prepared by an efficient and one-step reduction method, followed by heating in an argon (Ar) atmosphere at different temperatures (200−500 °C) to fabricate Ru_xCo_yBO-T nanocomposites (see Experimental Section for details). Electrocatalytic performances of Ru_xCo_yBO precursors with different Ru/Co atomic ratios have been tested first, and the Ru_2Co_1BO precursor that exhibits the best activity was used for further study (Table S1, Figure S1 and detailed description). A plot of the thermogravimetric analysis with differential scanning calorimetry (TG-DSC) data for Ru_2Co_1BO (Figure 1a) shows two exothermic peaks at 230 and 340 °C. From the data and X-ray diffraction (XRD) patterns (Figure 1b) of as-prepared Ru_2Co_1BO and those of composites generated by calcination at temperatures between 200 and 500 °C, we deduce a possible crystalline transformation of Ru−Co alloy at 230 °C and an oxidation phase transformation at 340 °C. For example, at calcination temperatures greater than 200 °C, the broad peak at 42.8° (Ru_2Co_1BO and Ru_2Co_1BO-200) shifts to 44.5°, which is located between standard diffraction peaks of Ru (101) (44.0°; JCPDS No. 06-0663) and Co (101) (47.3°; JCPDS No. 05-0727).[22,28] The peaks of Ru_2Co_1BO-300 and Ru_2Co_1BO-350 at 38.8° for the Ru−Co (100) planes and 44.5° for the Ru−Co (101) planes appeared and enhanced compared to those of Ru_2Co_1BO and Ru_2Co_1BO-200, indicating the crystallization enhancement of Ru−Co alloy after calcination. In addition, the peaks of Ru_xCo_yBO-350 showed a small shift to higher angles compared with those of RuBO-350 (Figure S2), which agreed with the characteristics of alloys in XRD peaks.[29,30] The XRD patterns of composites generated using calcination temperatures greater than 350 °C contain peaks associated with RuO_2 (JCPDS No. 43-1027),[31] which could be attributed to the crystallization of amorphous metal oxides (e.g., RuO_2) formed in the synthesis of Ru_xCo_yBO precursors.[25]

Because the Ru_2Co_1BO-350 nanocomposite has higher HER and OER performances than those of related catalysts (Figures S3 & S4, Table S2, and detailed description), it was used in further studies. Scanning electron microscopy (SEM) and transmission electron microscopy (TEM) display that Ru_2Co_1BO-350 is comprised of interconnected nanoparticles with sizes of ∼20 nm (Figures S5 and S6), which themselves are composed of much smaller particles with an average size of 3.9 nm (Figures 1c,d and S7). Owing to this secondary structural feature, Ru_2Co_1BO-350 has a specific surface area of 38 m^2 g^{-1} (Figure S8). The high-resolution TEM image (Figure 1d) shows that the particles have a lattice spacing of 0.20 and 0.21 nm, which matches those for the (101) and (002) planes of Ru−Co alloy and are consistent with the

https://doi.org/10.1021/acs.nanolett.2c04668
Nano Lett. 2023, 23, 1052−1060

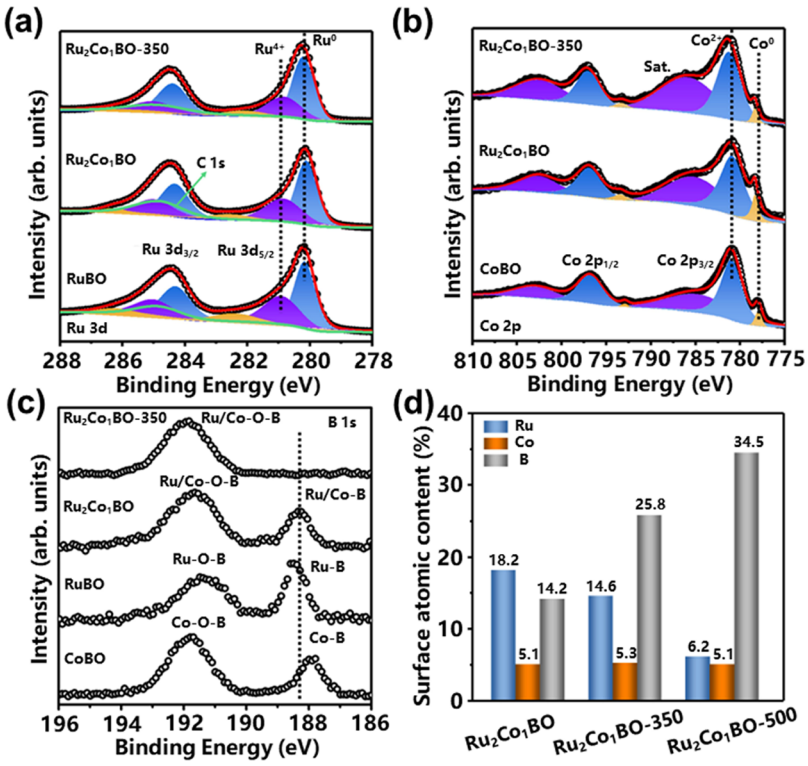

Figure 2. XPS spectra for CoBO, RuBO, Ru_2Co_1BO, and Ru_2Co_1BO-350 of (a) Ru 3d, (b) Co 2p, and (c) B 1s regions. (d) Surface atom content of Ru, Co, and B from XPS results.

results of selected area electron diffraction (SAED) (Figure 1c, inset). The high-angle annular dark-field scanning transmission electron microscope (HAADF-STEM) image and element surface distribution of Ru_2Co_1BO-350 (Figures 1e and S9) demonstrate that Ru, Co, B, and O atoms are distributed throughout the nanoparticles. The diffraction pattern (Figure 1f) of region I in Figure 1d from fast Fourier transformation (FFT) can be indexed to the (101) and (002) planes of a hexagonal closest-packed (hcp)-type Ru−Co alloy.[32] Crystal lattice fusion of Ru−Co nanoparticles in Ru_2Co_1BO-350 is observed in the inverse FFT image (Figure 1g) of the diffraction pattern in Figure 1f. Figure 1h is a magnification of region II in Figure 1g; the ordered lattice fringes are at the left and right regions, and the lattice distortions are in the middle region.

X-ray photoelectron spectroscopy (XPS) was performed to identify the elements present on the surface of Ru_2Co_1BO-350. The XPS spectra displayed in Figure 2a contain Ru $3d_{5/2}$ peaks for RuBO (280.2 eV), Ru_2Co_1BO (280.1 eV), and Ru_2Co_1BO-350 (280.2 eV), which all are ascribed to metallic Ru^0.[33] The presence of metallic Co^0 is confirmed by the presence of peaks for Co $2p_{3/2}$ at 778.4 eV (Ru_2Co_1BO and Ru_2Co_1BO-350) and 778.0 eV (CoBO) (Figure 2b).[34] The content ratios of Ru^{4+}/Ru^0, Co^{2+}/Co^0 are 0.5, 17.4, and 0.7, 5.5 of Ru_2Co_1BO-350 and Ru_2Co_1BO, respectively, indicating that the oxidation degree of cobalt increased on the surface of catalyst after calcination. The spectra in Figure 2c contain B 1s derived peaks for CoBO (187.9 eV), RuBO (188.5 eV), and Ru_2Co_1BO (188.3 eV).[25,35] However, after calcination, the signal associated with Ru−B or Co−B is no longer present, and only a peak at 191.9 eV corresponding to the binding energy of Ru−O−B or Co−O−B and B−O bonds in B_2O_3 remains.[35] The results demonstrate that more Ru/Co−O−B species formed in the calcination process, probably by oxidation of as-synthesized Ru_2Co_1BO.[36]

Interestingly, XPS data displays (Figures 2d and S10) that the B/metal element ratio in Ru_2Co_1BO-500 (3.1) is higher than those in Ru_2Co_1BO-350 (1.3) and as-synthesized Ru_2Co_1BO (0.6), which means that the content of surface B−O species increased relatively upon calcination and the formed B-rich surface is due to different diffusion behaviors of heavy elements of Co and Ru and light element of B at high temperature.[37] Furthermore, compared to the surface of a pure alloy, the one in the calcinated nanocomposites with more oxidized surface species should have favorable hydrophilicity (Figures S11 and S12 and detailed description). High hydrophilicity is a desirable property for seawater-splitting catalysts, which leads to accelerated water-adsorption/dissociation that improves performance and ion shielding that enhances stability.[38,39]

The HER and OER activities and stabilities of Ru_2Co_1BO-350 under different pH conditions were determined using a standard three-electrode system (Figures S13 & S14, Tables S3 & S4, and detailed description). In addition, the performance of Ru_2Co_1BO-350 in alkaline seawater was evaluated and compared with other catalysts including Ru_2Co_1 nanoalloy (Ru_2Co_1), nanostructured Ru (nano Ru), and RuBO-350 composite (detailed synthesis methods and structure characterization are given in the Supporting Information, Figures S15 and S16). Ru_2Co_1BO-350 exhibits the highest HER activity with overpotential of 14 mV at 10 mA cm^{-2} (denoted as η_{10} = 14 mV), which is superior to those of Ru_2Co_1 (η_{10} = 20 mV), nano Ru (η_{10} = 33 mV), Pt/C (η_{10} = 29 mV), and RuBO-350 (η_{10} = 32 mV) (Figures 3a,b & S17, Table S5). The findings indicate that introduction of B and alloying effects can promote the HER performance effectively. The Tafel slope

https://doi.org/10.1021/acs.nanolett.2c04668
Nano Lett. 2023, 23, 1052−1060

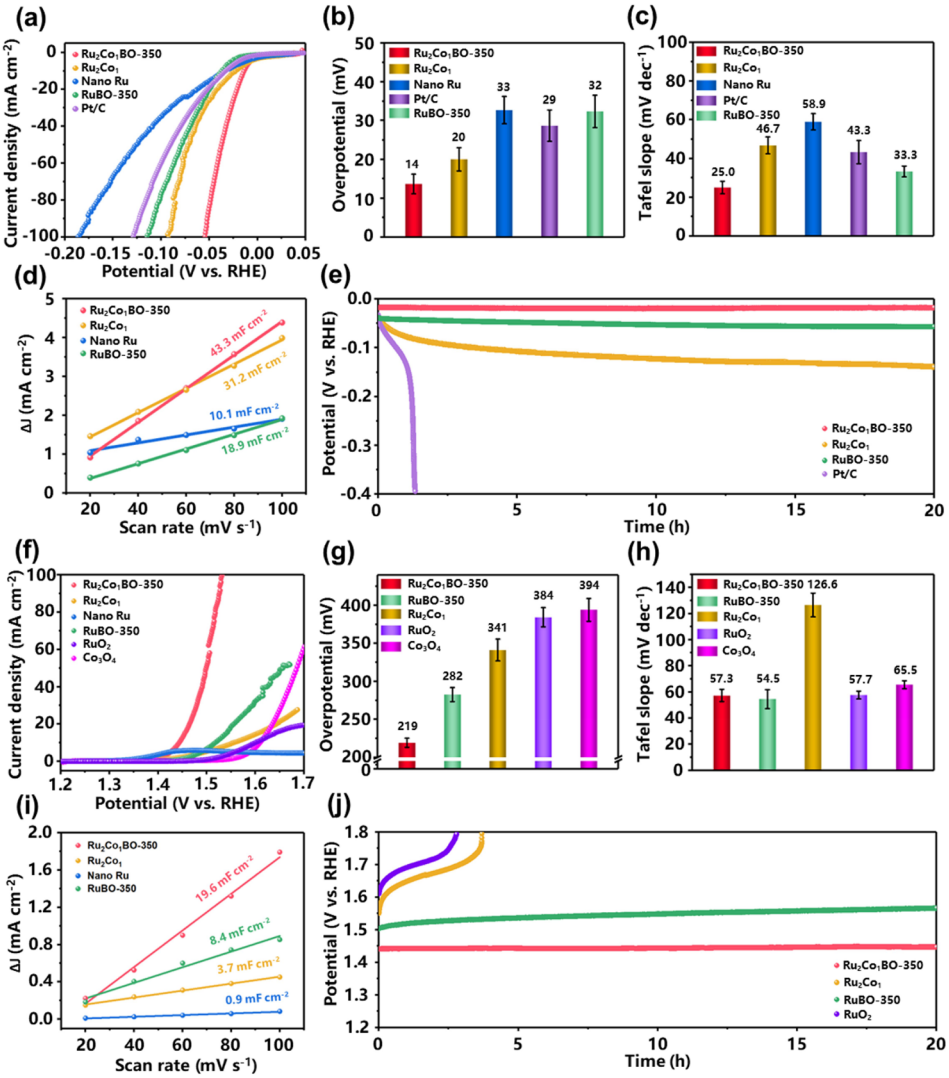

Figure 3. HER and OER performance of Ru_2Co_1BO-350, Ru_2Co_1, nano Ru, RuBO-350, Pt/C, RuO_2, and Co_3O_4 in alkaline seawater. (a) Polarization curves for HER. (b) Comparison of HER overpotential @10 mA cm^{-2}. (c) HER Tafel plots. (d) C_{dl} by linear fitting of scan-rate-dependent capacitance currents at 0.15 V (vs RHE). (e) Chronoamperometric test of Ru_2Co_1BO-350, Ru_2Co_1, RuBO-350, and Pt/C at the current density of 10 mA cm^{-2}. (f) Polarization curves for OER. (g) Comparison of OER overpotential @10 mA cm^{-2}. (h) OER Tafel plots. (i) C_{dl} by linear fitting of scan-rate-dependent capacitance currents at 1.25 V (vs RHE). (j) Chronoamperometric test of Ru_2Co_1BO-350, Ru_2Co_1, RuBO-350, and RuO_2 at the current density of 10 mA cm^{-2}.

of Ru_2Co_1BO-350 (25.0 mV dec^{-1}) suggests that the rate of the HER promoted by Ru_2Co_1BO-350 is larger than those of Pt/C (43.3 mV dec^{-1}), Ru_2Co_1 (46.7 mV dec^{-1}), and RuBO-350 (33.3 mV dec^{-1}) (Figures 3c & S17, Table S5). Also, Ru_2Co_1BO-350 displays the largest electrochemical double-layer capacitance (C_{dl}) (43.3 mF cm^{-2}), indicating that it possesses a greatly enhanced number of surface active sites (Figures 3d and S18). Nyquist plots demonstrate that Ru_2Co_1BO-350 has the lowest reaction resistance (Figure S19). Of equal importance is the observation that the nanocomposite that forms by introducing B enhances greatly the stability (Figure 3e), and Ru_2Co_1BO-350 shows much higher performance-price ratio than commercial Pt/C (Table S6 and detailed description).

In addition to high HER performance, Ru_2Co_1BO-350 also has an OER activity (η_{10} = 219 mV) that is much higher than those of Ru_2Co_1 (η_{10} = 341 mV), RuBO-350 (η_{10} = 282 mV), RuO_2 (η_{10} = 384 mV), and Co_3O_4 (η_{10} = 394 mV) in alkaline seawater (Figures 3f,g & S20, Table S7). The lower Tafel slope, larger C_{dl} value, and smaller R_{CT} value of Ru_2Co_1BO-350 compared to those of Ru_2Co_1, RuBO-350, and RuO_2 (Figures 3h,i & S18−S20, Table S7) clearly demonstrate the superiority of the B-containing, alloyed electrocatalyst. Furthermore, the results of a chronopotentiometric test of durability (Figure 3j) indicate that Ru_2Co_1BO-350 has the greatest resistance to corrosion.

The structure of Ru_2Co_1BO-350 was examined after it was used to promote the HER and OER for 20 h. The SEM images confirmed that the morphology of Ru_2Co_1BO-350 nanoparticles is retained (Figure S21). The XRD pattern (Figure S22) of this material after an HER stability test contains diffraction peaks for the Ru−Co alloy, while characteristic peaks of the metal are not present in XRD patterns on material subjected to an OER stability test. In addition, the XPS data demonstrate that the relative intensities of peaks ascribed to Ru^{4+} (463.3 eV, Figure 4a), Co^{2+} (781.4 eV, Figure 4b), and hydroxyl (531.2 eV, Figure 4c) after HER increased relative to those of original Ru_2Co_1BO-350 greatly, while signals

https://doi.org/10.1021/acs.nanolett.2c04668
Nano Lett. 2023, 23, 1052−1060

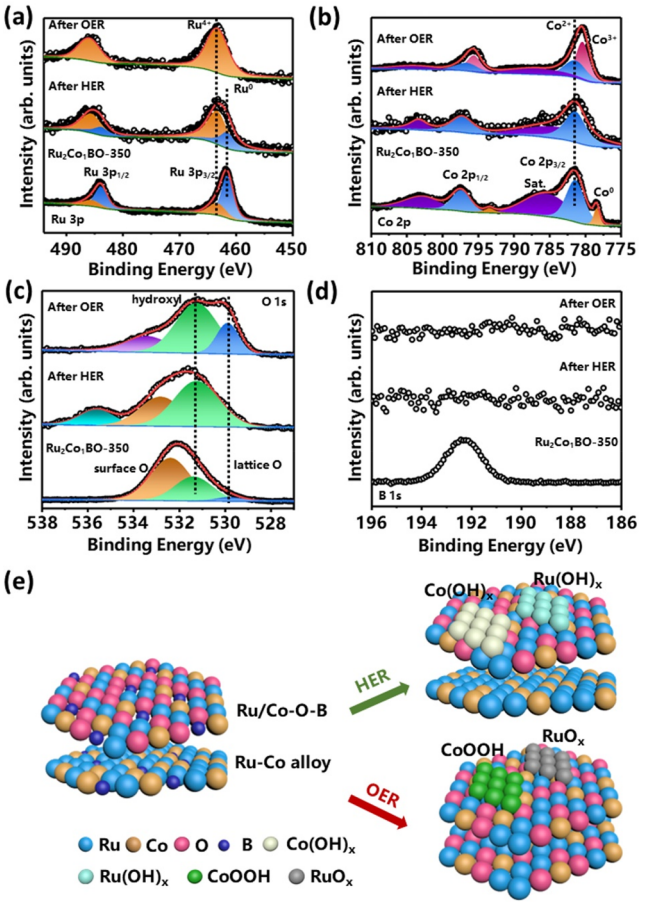

Figure 4. XPS spectra for Ru_2Co_1BO-350 and electrode of Ru_2Co_1BO-350 after HER and OER tests of (a) Ru 3p, (b) Co 2p, (c) O 1s, and (d) B 1s regions. (e) Schematic illustration of Ru_2Co_1BO-350 surface reconstructed in HER and OER.

associated with Co^0 and B species (Figure 4d) are no longer present after HER. These changes indicate that amorphous hydroxides (e.g., $Ru(OH)_x$ and $Co(OH)_x$) are formed on the surface structure during HER, and this process is accompanied by leaching of surface B species. $Co(OH)_x$ can promote dissociation of H_2O and formation of the hydrogen intermediate (H_{ad}),[40] which is strongly absorbed on pure Ru metal.[13] The surface OH groups of $Ru(OH)_x$ can make Ru less prone to bind H_{ad}, and the high conductivity of Ru metal can accelerate the electron transfer. These factors contribute to the excellent HER performance.

Similar changes also occur during the OER stability test, where Ru^0 and Co^0 in Ru_2Co_1BO-350 become oxidized to form the respective higher valence states Ru^{4+} (463.3 eV, Figure 4a), Co^{2+}, and Co^{3+} (781.4 and 780.4 eV, Figure 4b). Also, signals for lattice oxygen (529.9 eV) and hydroxyl groups (531.2 eV) appear in the XPS data after an OER test (Figure 4c). The results of Raman spectroscopy verify that CoOOH is generated (Figure S23). These results indicate that some amorphous oxides and (oxy)hydroxides (e.g., RuO_x and CoOOH) are formed during OER.[14] CoOOH is formed at a lower potential from Ru_2Co_1BO-350 than $Co(OH)_2$, which is possibly a result of the defect structure caused by leaching B species during OER (Figures 4d and S24). The lower overpotential for OER of the catalyst can protect Ru from being overoxidized, and the generated RuO_x-CoOOH becomes fixed to Ru on the surface creating high stability.[41] In addition, the CoOOH can optimize the oxygen-binding energy of Ru sites and improve the OER performance.[42] Thus, the surface reconstruction of Ru_2Co_1BO-350 during the HER and OER can be schematically illustrated in Figure 4e.

Two-electrode water/seawater splitting devices were assembled with Ru_2Co_1BO-350 as electrodes. The Ru_2Co_1BO-350 ‖ Ru_2Co_1BO-350-based device exhibits excellent activity with a voltage of 1.466 V at 10 mA cm^{-2}, and this voltage does not decay over at least 110 h (Figures 5a,b & S25), which is far superior to those of Ru_2Co_1 ‖ Ru_2Co_1 (1.510 V) and Pt/C ‖ RuO_2 (1.544 V). Assessments of performances under high current densities of 50 and 100 mA cm^{-2} show the high stability of the catalyst over a 230 h period (Figure 5b), and the interconnected nanoparticle structure of Ru_2Co_1BO-350 was retained (Figure S26). The surface reconstruction of Ru_2Co_1BO-350 electrode was further confirmed after high current densities tests, and no signal of Cl was detected, which implies a high resistance to Cl^- corrosion (Figure S27 and detailed description). The Ru_2Co_1BO-350 ‖ Ru_2Co_1BO-350 device also displays high performance and durability in overall water splitting over a broad pH range (Figure S28 and detailed description). The remarkable performance of this two-electrode system is comparable to those of other prominent electrocatalysts (Figure 5c, Tables S8 & S9).

The Ru_2Co_1BO-350-based two-electrode seawater splitting device was then paired with a commercial Si solar cell to assess its performance in sun light-driven seawater splitting (Figure S29). By monitoring the volume of gas produced every 10 min, the volume ratio of H_2 to O_2 generated was estimated to be 2.004:1, which is close to the theoretical value for seawater electrolysis (Figure S30), and the calculated Faradaic efficiency is ~98.6% (Figures 5d & S31, Table S10, and detailed description). The collected gas from the anode was analyzed by mass spectrometry (MS); O_2 was clearly identified, while no signal of Cl_2 was detected (Figure 5e). Furthermore, the electrolytes were subjected to an *o*-tolidine indicator test after we carried out an OER stability test for 20 h at 10 mA cm^{-2} using Ru_2Co_1BO-350, Ru_2Co_1, and RuO_2; the electrolyte of Ru_2Co_1BO-350 ‖ Ru_2Co_1BO-350 after seawater splitting tests at 50 and 100 mA cm^{-2} was also tested.[43] No characteristic adsorption peaks were observed in the UV−vis spectrum of the colorless electrolyte of Ru_2Co_1BO-350, while the color of the electrolyte of Ru_2Co_1 and RuO_2 are yellow in association with absorption peaks in their UV−vis spectra around 437 nm (Figure S32 and detailed description). These results indicate that the Ru_2Co_1BO-350 can effectively avoid the generation of Cl_2 and ClO^- during seawater electrolysis. Moreover, density functional theory (DFT) calculations were conducted to gain information about why the Ru_2Co_1BO-350 prevented the chlorine evolution reaction (CER) in alkaline seawater. Ru_2Co_1BO-350 (RuO_2/CoOOH, Figure S33) and RuO_2 (Figure S34) were utilized as models in the calculations. The calculated charge density and differential charge density distributions show that the electron densities at O sites in RuO_2/CoOOH are more polarized than those in RuO_2 (Figures 5f,g and S35). The redistribution of charge on O sites can influence adsorption of Cl^-. In addition, the partial density of states (PDOS) of O and Ru at the Fermi level in RuO_2/CoOOH are lower than those of RuO_2 (Figure 5h,i), implying that reduced electron mobility takes place during the CER, which prevents a side reaction. As is shown in Figure 5j, the Gibbs adsorption energy (ΔG_{ads}) of intermediate Cl* on the RuO_2/CoOOH of activated Ru_2Co_1BO-350 surface is 1.16

https://doi.org/10.1021/acs.nanolett.2c04668
Nano Lett. 2023, 23, 1052−1060

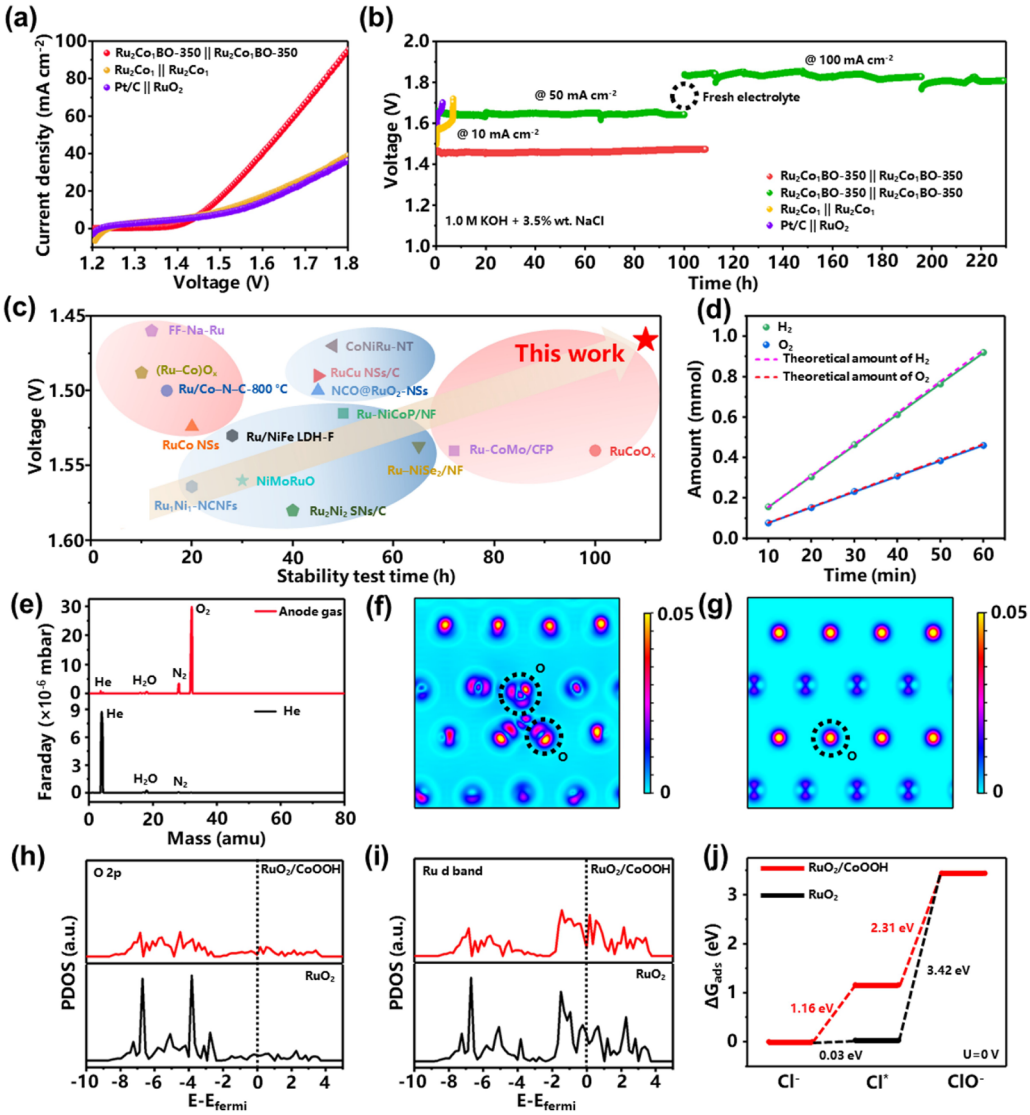

Figure 5. Overall alkaline seawater splitting of Ru_2Co_1BO-350 ‖ Ru_2Co_1BO-350, Ru_2Co_1 ‖ Ru_2Co_1, and Pt/C ‖ RuO_2. (a) Polarization curves. (b) Long-term stability at the current density of 10, 50, and 100 mA cm^{-2}. (c) Comparison of the voltage and stability between Ru_2Co_1BO-350 and other reported catalysts for water splitting in alkaline media. (d) Comparison between the amount of collected gaseous products and theoretical amount of gases. (e) The mass spectra of collected anode gas and carrier gas (He). Charge density distributions in models of (f) RuO_2/CoOOH and (g) RuO_2. PDOS of (h) O 2p and (i) Ru d band in RuO_2/CoOOH and RuO_2. (j) The Gibbs free energy diagram of the indicated sample (RuO_2/CoOOH and RuO_2) during the ClO^- formation process.

eV, which is much larger than that of RuO_2 (0.03 eV). It further indicates that the Cl^- is more difficult to be adsorbed on the RuO_2/CoOOH surface than that of RuO_2. Therefore, compared to a pure RuO_2 surface, the reconstructed surface of Ru_2Co_1BO-350 exhibits enhanced resistance to Cl^- corrosion. The results suggest that the Ru_2Co_1BO-350-based electrolysis device has excellent stability for seawater splitting into H_2 and O_2, and it highly resists Cl^- corrosion.

The remarkable electrocatalytic activity and stability of Ru_2Co_1BO-350 can thus be attributed to (1) the surface oxide species on the catalyst, which improves surface hydrophilicity for enhanced water adsorption to promote the water involved reactions, (2) reconstruction of the active surfaces during the electrocatalytic processes, which can not only promote dissociation of H_2O but also optimize the electronic structure of Ru for an appropriate adsorption of intermediates in both HER and OER, and (3) the low OER overpotential apparently alleviates further oxidation of Ru^{4+}, formed from Ru during the OER, to generate unstable RuO_4; instead, RuO_x-CoOOH that is generated helps to prevent Cl^- corrosion and improve the stability of Ru.

In summary, Ru_2Co_1BO-350 is an efficient and stable electrocatalyst for seawater splitting, and it can be fabricated using a facile method involving reduction and low-temperature calcination. Surface reconstruction of Ru_2Co_1BO-350 during HER and OER have been evidenced, and the generated active surfaces, Ru/$Ru(OH)_x$/$Co(OH)_x$ in HER and RuO_x-CoOOH in OER, are the critical factors for enhancement of the electrocatalytic performance and the resistance to seawater-induced corrosion. The results of this study have both fundamental and practical importance in that they demonstrate a facile strategy exists for improving the activities and stabilities of Ru-based nanocomposites as both anodes and cathodes in a seawater/water splitting device.

https://doi.org/10.1021/acs.nanolett.2c04668
Nano Lett. 2023, 23, 1052−1060

■ ASSOCIATED CONTENT

Supporting Information

The Supporting Information is available free of charge at https://pubs.acs.org/doi/10.1021/acs.nanolett.2c04668.

Details of materials, structural characterization, electrochemical performances and computational studies, additional characterizations include ICP-AES, XRD, TEM, EDS, SEM, XPS, LSV polarization curves, UV−vis spectra, and theoretical calculations of the models for CER performance (PDF)

Video of seawater splitting catalyzed by Ru_2Co_1BO-350 through a solar cell-driven electrolysis (MP4)

■ AUTHOR INFORMATION

Corresponding Author

Xiao-Yu Yang − *State Key Laboratory of Advanced Technology for Materials Synthesis and Processing, and International School of Materials Science & Engineering, and School of Materials Science & Engineering, and Shenzhen Research Institute, and Joint Laboratory for Marine Advanced Materials in Pilot National Laboratory for Marine Science and Technology (Qingdao), Wuhan University of Technology, 430070 Wuhan, Hubei, China;* orcid.org/0000-0003-3454-3604; Email: xyyang@whut.edu.cn

Authors

Le-Wei Shen − *State Key Laboratory of Advanced Technology for Materials Synthesis and Processing, and International School of Materials Science & Engineering, and School of Materials Science & Engineering, and Shenzhen Research Institute, and Joint Laboratory for Marine Advanced Materials in Pilot National Laboratory for Marine Science and Technology (Qingdao), Wuhan University of Technology, 430070 Wuhan, Hubei, China*

Yong Wang − *State Key Laboratory of Advanced Technology for Materials Synthesis and Processing, and International School of Materials Science & Engineering, and School of Materials Science & Engineering, and Shenzhen Research Institute, and Joint Laboratory for Marine Advanced Materials in Pilot National Laboratory for Marine Science and Technology (Qingdao), Wuhan University of Technology, 430070 Wuhan, Hubei, China*

Jiang-Bo Chen − *State Key Laboratory of Advanced Technology for Materials Synthesis and Processing, and International School of Materials Science & Engineering, and School of Materials Science & Engineering, and Shenzhen Research Institute, and Joint Laboratory for Marine Advanced Materials in Pilot National Laboratory for Marine Science and Technology (Qingdao), Wuhan University of Technology, 430070 Wuhan, Hubei, China*

Ge Tian − *State Key Laboratory of Advanced Technology for Materials Synthesis and Processing, and International School of Materials Science & Engineering, and School of Materials Science & Engineering, and Shenzhen Research Institute, and Joint Laboratory for Marine Advanced Materials in Pilot National Laboratory for Marine Science and Technology (Qingdao), Wuhan University of Technology, 430070 Wuhan, Hubei, China*

Kang-Yi Xiong − *State Key Laboratory of Advanced Technology for Materials Synthesis and Processing, and International School of Materials Science & Engineering, and School of Materials Science & Engineering, and Shenzhen Research Institute, and Joint Laboratory for Marine Advanced Materials in Pilot National Laboratory for Marine Science and Technology (Qingdao), Wuhan University of Technology, 430070 Wuhan, Hubei, China*

Christoph Janiak − *Institut für Anorganische Chemie und Strukturchemie, Heinrich-Heine-Universität Düsseldorf, 40204 Düsseldorf, Germany;* orcid.org/0000-0002-6288-9605

David Cahen − *Department of Chemistry, and Bar-Ilan Institute for Nanotechnology & Advanced Materials, Bar-Ilan University, 5290002 Ramat Gan, and Department of Molecular Chemistry & Materials Science, Weizmann Institute of Science, 76100 Rehovot, Israel;* orcid.org/0000-0001-8118-5446

Complete contact information is available at: https://pubs.acs.org/10.1021/acs.nanolett.2c04668

Author Contributions

[‖]L.-W.S. and Y.W. contributed equally to this work. L.-W.S., Y.W., and K.-Y.X. did the experiments of synthesis and electrocatalytic performance. X.-Y.Y. conceived the project and provided the idea. L.-W.S. and Y.W. designed the experiments and analyzed the data. G.T. performed the TEM and EDS characterizations. J.-B.C. performed the DFT calculation and analysis. L.-W.S., Y.W., and X.-Y.Y. wrote and revised the paper. C.J. and D.C. revised the paper. All of the authors discussed results, analyzed the data, and have given approval to the final version of the manuscript.

Notes

The authors declare no competing financial interest.

■ ACKNOWLEDGMENTS

This study was supported by National Key Research and Development Program of China (2022YFB3805600, 2022YFB3805604, 2022YFB3806800), National Natural Science Foundation of China (22293020), National 111 project (B20002), PCSIRT (IRT_15R52), Program Fund of Non-Metallic Excellence and Innovation Center for Building Materials (2023TDA1-1), Sino-German Center COVID-19 Related Bilateral Collaborative Project (C-0046), Guangdong Basic and Applied Basic Research Foundation (2022A151-5010137, 2022A1515010504), Shenzhen Science and Technology Program (JCYJ20210324142010029, GJHZ202107-05143204014, KCXFZ20211020170006010). We thank the Nanostructure Research Centre (NRC) for performing the S/TEM imaging.

■ REFERENCES

(1) Jin, H.; Wang, X.; Tang, C.; Vasileff, A.; Li, L.; Slattery, A.; Qiao, S. Z. Stable and Highly Efficient Hydrogen Evolution from Seawater Enabled by an Unsaturated Nickel Surface Nitride. *Adv. Mater.* **2021**, *33* (13), 2007508.

(2) Chen, J.-B.; Ying, J.; Xiao, Y.-X.; Dong, Y.; Ozoemena, K. I.; Lenaerts, S.; Yang, X.-Y. Stoichiometry Design in Hierarchical CoNiFe Phosphide for Highly Efficient Water Oxidation. *Sci. China Mater.* **2022**, *65*, 2685−2693.

(3) Dresp, S.; Dionigi, F.; Klingenhof, M.; Strasser, P. Direct Electrolytic Splitting of Seawater: Opportunities and Challenges. *ACS Energy Lett.* **2019**, *4*, 933−942.

(4) Yu, L.; Wu, L.; McElhenny, B.; Song, S.; Luo, D.; Zhang, F.; Yu, Y.; Chen, S.; Ren, Z. Ultrafast Room-temperature Synthesis of Porous S-doped Ni/Fe (oxy)Hydroxide Electrodes for Oxygen Evolution

Catalysis in Seawater Splitting. *Energy Environ. Sci.* **2020**, *13*, 3439−3446.
(5) Yang, Y.; Wu, D.; Yu, Y.; Li, J.; Rao, P.; Jia, C.; Liu, Z.; Chen, Q.; Huang, W.; Luo, J.; Deng, P.; Shen, Y.; Tian, X. Bridge the Activity and Durability of Ruthenium for Hydrogen Evolution Reaction with the RuOC Link. *Chem. Eng., J.* **2022**, *433*, 134421.
(6) Wang, S.; Wang, M.; Liu, Z.; Liu, S.; Chen, Y.; Li, M.; Zhang, H.; Wu, Q.; Guo, J.; Feng, X.; Chen, Z.; Pan, Y. Synergetic Function of the Single-Atom Ru−N_4 Site and Ru Nanoparticles for Hydrogen Production in a Wide pH Range and Seawater Electrolysis. *ACS Appl. Mater. Interfaces* **2022**, *14*, 15250−15258.
(7) Wu, D.; Kusada, K.; Yoshioka, S.; Yamamoto, T.; Toriyama, T.; Matsumura, S.; Chen, Y.; Seo, O.; Kim, J.; Song, C.; Hiroi, S.; Sakata, O.; Ina, T.; Kawaguchi, S.; Kubota, Y.; Kobayashi, H.; Kitagawa, H. Efficient Overall Water Splitting in Acid with Anisotropic Metal Nanosheets. *Nat. Commun.* **2021**, *12*, 1145.
(8) Cherevko, S.; Geiger, S.; Kasian, O.; Kulyk, N.; Grote, J.-P.; Savan, A.; Shrestha, B. R.; Merzlikin, S.; Breitbach, B.; Ludwig, A.; Mayrhofer, K. J. J. Oxygen and Hydrogen Evolution Reactions on Ru, RuO_2, Ir, and IrO_2 Thin Film Electrodes in Acidic and Alkaline Electrolytes: A Comparative Study on Activity and Stability. *Catal. Today* **2016**, *262*, 170−180.
(9) Kuang, Y.; Kenney, M. J.; Meng, Y.; Hung, W. H.; Liu, Y.; Huang, J. E.; Prasanna, R.; Li, P.; Li, Y.; Wang, L.; Lin, M. C.; McGehee, M. D.; Sun, X.; Dai, H. Solar-driven, Highly Sustained Splitting of Seawater into Hydrogen and Oxygen Fuels. *Proc. Natl. Acad. Sci. U S A* **2019**, *116*, 6624−6629.
(10) Reier, T.; Oezaslan, M.; Strasser, P. Electrocatalytic Oxygen Evolution Reaction (OER) on Ru, Ir, and Pt Catalysts: A Comparative Study of Nanoparticles and Bulk Materials. *ACS Catal.* **2012**, *2*, 1765−1772.
(11) Kim, B. J.; Abbott, D. F.; Cheng, X.; Fabbri, E.; Nachtegaal, M.; Bozza, F.; Castelli, I. E.; Lebedev, D.; Schäublin, R.; Copéret, C.; Graule, T.; Marzari, N.; Schmidt, T. J. Unraveling Thermodynamics, Stability, and Oxygen Evolution Activity of Strontium Ruthenium Perovskite Oxide. *ACS Catal.* **2017**, *7*, 3245−3256.
(12) Song, H. J.; Yoon, H.; Ju, B.; Kim, D. W. Highly Efficient Perovskite-Based Electrocatalysts for Water Oxidation in Acidic Environments: A Mini Review. *Adv. Energy Mater.* **2021**, *11*, 2002428.
(13) Shan, J.; Ling, T.; Davey, K.; Zheng, Y.; Qiao, S. Z. Transition-Metal-Doped RuIr Bifunctional Nanocrystals for Overall Water Splitting in Acidic Environments. *Adv. Mater.* **2019**, *31*, 1900510.
(14) Wang, C.; Qi, L. Heterostructured Inter-Doped Ruthenium−Cobalt Oxide Hollow Nanosheet Arrays for Highly Efficient Overall Water Splitting. *Angew. Chem., Int. Ed.* **2020**, *59*, 17219−17224.
(15) Pang, B.; Liu, X.; Liu, T.; Chen, T.; Shen, X.; Zhang, W.; Wang, S.; Liu, T.; Liu, D.; Ding, T.; Liao, Z.; Li, Y.; Liang, C.; Yao, T. Laser-assisted High-performance PtRu Alloy for pH-universal Hydrogen Evolution. *Energy Environ. Sci.* **2022**, *15*, 102−108.
(16) Xiao, Y. X.; Ying, J.; Tian, G.; Zhang, X. Q.; Janiak, C.; Ozoemena, K. I.; Yang, X. Y. PtPd Hollow Nanocubes with Enhanced Alloy Effect and Active Facets for Efficient Methanol Oxidation Reaction. *Chem. Commun.* **2021**, *57*, 986−989.
(17) Xiao, Y. X.; Ying, J.; Tian, G.; Yang, X.; Zhang, Y. X.; Chen, J. B.; Wang, Y.; Symes, M. D.; Ozoemena, K. I.; Wu, J. S.; Yang, X. Y. Hierarchically Fractal PtPdCu Sponges and their Directed Mass-and Electron-transfer Effects. *Nano Lett.* **2021**, *21* (18), 7870−7878.
(18) Cai, J.; Ding, J.; Wei, D.; Xie, X.; Li, B.; Lu, S.; Zhang, J.; Liu, Y.; Cai, Q.; Zang, S. Coupling of Ru and O-Vacancy on 2D Mo-Based Electrocatalyst Via a Solid-Phase Interface Reaction Strategy for Hydrogen Evolution Reaction. *Adv. Energy Mater.* **2021**, *11*, 2100141.
(19) Xiao, Y.-X.; Ying, J.; Tian, G.; Tao, Y.; Wei, H.; Fan, S.-Y.; Sun, Z.-H.; Zou, W.-J.; Hu, J.; Chang, G.-G.; Li, W.; Yang, X.-Y.; Janiak, C. Highly Dispersed PtPd on Graphitic Nanofibers and its Heavy d-π Effect. *Appl. Catal., B* **2019**, *259*, 118080.
(20) Alarawi, A.; Ramalingam, V.; He, J.-H. Recent Advances in Emerging Single Atom Confined Two-dimensional Materials for Water Splitting Applications. *Mater. Today Energy* **2019**, *11*, 1−23.
(21) Shen, L.; Ying, J.; Ozoemena, K. I.; Janiak, C.; Yang, X. Y. Confinement Effects in Individual Carbon Encapsulated Nonprecious Metal-Based Electrocatalysts. *Adv. Funct. Mater.* **2022**, *32* (15), 2110851.
(22) Zhu, T.; Huang, J.; Huang, B.; Zhang, N.; Liu, S.; Yao, Q.; Haw, S. C.; Chang, Y. C.; Pao, C. W.; Chen, J. M.; Shao, Q.; Hu, Z.; Ma, Y.; Huang, X. High-Index Faceted RuCo Nanoscrews for Water Electrosplitting. *Adv. Energy Mater.* **2020**, *10*, 2002860.
(23) Yu, J.; He, Q.; Yang, G.; Zhou, W.; Shao, Z.; Ni, M. Recent Advances and Prospective in Ruthenium-based Materials for Electrochemical Water Splitting. *ACS Catal.* **2019**, *9*, 9973−10011.
(24) Chen, D.; Liu, T.; Wang, P.; Zhao, J.; Zhang, C.; Cheng, R.; Li, W.; Ji, P.; Pu, Z.; Mu, S. Ionothermal Route to Phase-Pure RuB_2 Catalysts for Efficient Oxygen Evolution and Water Splitting in Acidic Media. *ACS Energy Lett.* **2020**, *5*, 2909−2915.
(25) Masa, J.; Weide, P.; Peeters, D.; Sinev, I.; Xia, W.; Sun, Z.; Somsen, C.; Muhler, M.; Schuhmann, W. Amorphous Cobalt Boride (Co_2B) as a Highly Effi cient Nonprecious Catalyst for Electrochemical Water Splitting: Oxygen and Hydrogen Evolution. *Adv. Energy. Mater.* **2016**, *6*, 1502313.
(26) Gupta, S.; Patel, M. K.; Miotello, A.; Patel, N. Metal Boride-based Catalysts for Electrochemical Water-splitting: A Review. *Adv. Funct. Mater.* **2020**, *30* (1), 1906481.
(27) Nsanzimana, J. M. V.; Gong, L.; Dangol, R.; Reddu, V.; Jose, V.; Xia, B. Y.; Yan, Q.; Lee, J. M.; Wang, X. Tailoring of Metal Boride Morphology via Anion for Efficient Water Oxidation. *Adv. Energy Mater.* **2019**, *9*, 1901503.
(28) Gao, Z.; Fan, G.; Liu, M.; Yang, L.; Li, F. Dandelion-like Cobalt Oxide Microsphere-supported RuCo Bimetallic Catalyst for Highly Efficient Hydrogenolysis of 5-Hydroxymethylfurfural. *Appl. Catal. B: environ.* **2018**, *237*, 649−659.
(29) Xiao, Y.-X.; Ying, J.; Chen, J.-B.; Dong, Y.; Yang, X.; Tian, G.; Wu, J.; Janiak, C.; Ozoemena, K. I.; Yang, X.-Y. Confined Ultrafine Pt in Porous Carbon Fibers and their N-enhanced Heavy d-π Effect. *Chem. Mater.* **2022**, *34*, 3705−3714.
(30) Wang, Y.; Yu, H. Z.; Ying, J.; Tian, G.; Liu, Y.; Geng, W.; Hu, J.; Lu, Y.; Chang, G. G.; Ozoemena, K. I.; Janiak, C.; Yang, X. Y. Ultimate Corrosion to Pt-Cu Electrocatalysts for Enhancing Methanol Oxidation Activity and Stability in Acidic Media. *Chem.-Eur. J.* **2021**, *27*, 9124−9128.
(31) Zhang, L.; Jang, H.; Liu, H.; Kim, M. G.; Yang, D.; Liu, S.; Liu, X.; Cho, J. Sodium-Decorated Amorphous/Crystalline RuO_2 with Rich Oxygen Vacancies: A Robust pH-Universal Oxygen Evolution Electrocatalyst. *Angew. Chem., Int. Ed.* **2021**, *60*, 18821−18829.
(32) Zhang, Q.; Kusada, K.; Wu, D.; Yamamoto, T.; Toriyama, T.; Matsumura, S.; Kawaguchi, S.; Kubota, Y.; Kitagawa, H. Selective Control of fcc and hcp Crystal Structures in Au−Ru Solid-solution Alloy Nanoparticles. *Nat. Commun.* **2018**, *9*, 510.
(33) Morgan, D. J. Resolving Ruthenium: XPS Studies of Common Ruthenium Materials. *Surf. Interface Anal.* **2015**, *47*, 1072−1079.
(34) Li, W.; Zhao, Y.; Liu, Y.; Sun, M.; Waterhouse, G. I. N.; Huang, B.; Zhang, K.; Zhang, T.; Lu, S. Exploiting Ru-induced Lattice Strain in CoRu Nanoalloys for Robust Bifunctional Hydrogen Production. *Angew. Chem., Int. Ed.* **2021**, *60*, 3290−3298.
(35) Jiang, W. J.; Niu, S.; Tang, T.; Zhang, Q. H.; Liu, X. Z.; Zhang, Y.; Chen, Y. Y.; Li, J. H.; Gu, L.; Wan, L. J.; Hu, J. S. Crystallinity-Modulated Electrocatalytic Activity of a Nickel(II) Borate Thin Layer on Ni_3B for Efficient Water Oxidation. *Angew. Chem., Int. Ed.* **2017**, *56*, 6572−6577.
(36) Geng, J.; Jefferson, D. A.; Johnson, B. F. G. The Unusual Nanostructure of Nickel−boron Catalyst. *Chem. Commun.* **2007**, 969−971.
(37) Li, L.; Tang, C.; Cui, X.; Zheng, Y.; Wang, X.; Xu, H.; Zhang, S.; Shao, T.; Davey, K.; Qiao, S. Z. Efficient Nitrogen Fixation to Ammonia through Integration of Plasma Oxidation with Electrocatalytic Reduction. *Angew. Chem., Int. Ed.* **2021**, *60*, 14131−14137.
(38) Xiao, S.-T.; Wu, S.-M.; Dong, Y.; Liu, J.-W.; Wang, L.-Y.; Wu, L.; Zhang, Y.-X.; Tian, G.; Janiak, C.; Shalom, M.; Wang, Y.-T.; Li, Y.-Z.; Jia, R.-K.; Bahnemann, D. W.; Yang, X.-Y. Rich Surface Hydroxyl

Design for Nanostructured TiO_2 and its Hole-trapping Effect. *Chem. Eng. J.* **2020**, *400*, 125909.
(39) Zhang, Y. X.; Wu, S. M.; Tian, G.; Zhao, X. F.; Wang, L. Y.; Yin, Y. X.; Wu, L.; Li, Q. N.; Zhang, Y. X.; Wu, J. S.; Janiak, C.; Ozoemena, K. I.; Shalom, M.; Yang, X. Y. Titanium Vacancies in TiO_2 Nanofibers Enable Highly Efficient Photodriven Seawater Splitting. *Chem.-Eur. J.* **2021**, *27* (57), 14202−14208.
(40) Subbaraman, R.; Tripkovic, D.; Strmcnik, D.; Chang, K.; Uchimura, M.; Paulikas, A. P.; Stamenkovic, V.; Markovic, N. M. Enhancing Hydrogen Evolution Activity in Water Splitting by Tailoring Li^+-$Ni(OH)_2$-Pt Interfaces. *Science* **2011**, *334*, 1256−1260.
(41) Li, P.; Wang, M.; Duan, X.; Zheng, L.; Cheng, X.; Zhang, Y.; Kuang, Y.; Li, Y.; Ma, Q.; Feng, Z.; Liu, W.; Sun, X. Boosting Oxygen Evolution of Single-atomic Ruthenium through Electronic Coupling with Cobalt-iron Layered Double Hydroxides. *Nat. Commun.* **2019**, *10* (1), 1−11.
(42) Liu, J.; Zheng, Y.; Jiao, Y.; Wang, Z.; Lu, Z.; Vasileff, A.; Qiao, S. Z. NiO as a Bifunctional Promoter for RuO_2 toward Superior Overall Water Splitting. *Small* **2018**, *14*, 1704073.
(43) Hsu, S. H.; Miao, J.; Zhang, L.; Gao, J.; Wang, H.; Tao, H.; Hung, S. F.; Vasileff, A.; Qiao, S. Z.; Liu, B. An Earth-abundant Catalyst-based Seawater Photoelectrolysis System with 17.9% Solar-to-Hydrogen Efficiency. *Adv. Mater.* **2018**, *30* (18), 1707261.

https://doi.org/10.1021/acs.nanolett.2c04668
Nano Lett. 2023, 23, 1052−1060